RSC Advances

PAPER

View Article Online
View Journal | View Issue

Open Access Article. Published on 12 May 2025. Downloaded on 10/31/2025 12:40:26 PM.
This article is licensed under a Creative Commons Attribution-NonCommercial 3.0 Unported Licence.

Check for updates

Cite this: *RSC Adv.*, 2025, **15**, 15609

Misorientation statistics across hot-deformed $Nd_2Fe_{14}B$ permanent magnet boundaries and the potential correlation with magnetic properties

Qian Li[ab] and Yuan Teng *[c]

In this study, planar electron backscatter diffraction data of hot-deformed (HD) $Nd_2Fe_{14}B$ magnets were analyzed to investigate the misorientation relationships on the grain boundary plane. The potential correlation between the misorientation angles of $Nd_2Fe_{14}B/Nd_2Fe_{14}B$ grain boundaries (Nd/Nd boundaries) and $Nd_2Fe_{14}B$/Nd-rich phase boundaries (Nd/Nr boundaries) was explored, along with their impact on the properties of the magnets. The characteristics of the grain boundary plane distribution of specific preferred misorientation angles were also investigated. The results revealed that the Nd/Nd boundaries exhibited preferred misorientation angles of 45° and 56°, whereas the Nd/Nr boundaries showed angles of 45° and 62°. The 45° grain boundary plane preferred the (001) orientation, and the 56° grain boundary plane favored the (122) orientation, and the 62° grain boundary plane preferred the (010) orientation. By integrating materials science and computational science, this study improves the understanding of the interface structure and properties of HD Nd–Fe–B magnets.

Received 23rd January 2025
Accepted 16th April 2025

DOI: 10.1039/d5ra00545k

rsc.li/rsc-advances

1. Introduction

Nd–Fe–B is a critical rare-earth magnet material, and its anisotropy is a key focus in engineering applications. The anisotropy of rare earth permanent magnets can be categorized into three types: (1) directional anisotropy, including anisotropy in the easy and hard magnetization directions,[1] and anisotropy along specific crystal axes;[2] (2) interface anisotropy, encompassing anisotropy at the interfaces,[3] annealing effects,[4] and exchange coupling;[5] and (3) strain anisotropy, which includes magnetoelastic coupling[6] and anisotropy induced by stresses and strains in the material.[7] In Nd–Fe–B materials, the grain boundary plane plays a significant role in the material's properties. This plane consists of two components: (1) the boundary between Nd–Fe–B grains and (2) the boundary between Nd–Fe–B and Nd-rich phases. Specifically, Nd–Fe–B materials feature a grain boundary network that includes both Nd–Fe–B/Nd–Fe–B grain boundaries and Nd–Fe–B/Nd-rich phase boundaries.[8] However, a research gap exists regarding the anisotropy at the grain and phase boundaries. Thus, investigating these boundaries is important for three reasons: (1) from a structural perspective, the smaller the Nd–Fe–B grains are, the larger the interfacial area becomes, making the interface a critical structural factor; (2) from the standpoint of interfacial structure, understanding how anisotropy, characterized by misorientation in this study, at the grain and phase boundaries affects material properties, is essential, as this relationship is not yet fully understood; and (3) from a processing perspective, Nd–Fe–B permanent magnets prepared by spark plasma sintering (SPS) exhibit differences in interfacial structure, anisotropy, and magnetic properties due to variations in interfacial weight, warranting further investigations.

The SPS technique utilizes high-frequency transient, localized high-temperature fields to heat Nd–Fe–B permanent magnets *via* pulse energy, Joule heating, and spark-induced pressure.[9,10] The grain size of Nd–Fe–B permanent magnets is consistently small, predominantly exhibiting an equiaxed morphology, suggesting that shape anisotropy is not well developed. The special electric current sintering process also affects the wetting and penetration of the Nd-rich phase into the main $Nd_2Fe_{14}B$ phase.[11] However, the Nd-rich phase may not always reach equilibrium following rapid sintering.[12] Additionally, severe plastic deformation can result in an uneven distribution of the Nd-rich phase.[13] Therefore, investigating the influence of the $Nd_2Fe_{14}B$ and Nd-rich phase combination on texture formation is an important research topic. Over the past few decades, research characterizing texture as intrinsic anisotropy has become increasingly comprehensive and detailed.[14–17] However, few studies have investigated the impact of the Nd–Fe–B interface on texture and anisotropy. This study, therefore, addresses these gaps by focusing on these issues. It represents an interdisciplinary approach that combines stereology with the interface structure of permanent magnet

[a]*Innovation and Practice Base for Postdoctors, Chengdu Polytechnic, Chengdu 610041, P. R. China*
[b]*Sichuan Provincial Engineering Research Center of Thermoelectric Materials and Devices, Chengdu Polytechnic, Chengdu 610041, P. R. China*
[c]*School of Materials Science and Engineering, Guangdong Ocean University, Yangjiang 529500, P. R. China. E-mail: tengyuan@gdou.edu.cn*

© 2025 The Author(s). Published by the Royal Society of Chemistry

Open Access Article. Published on 12 May 2025. Downloaded on 10/31/2025 12:40:26 PM.
This article is licensed under a Creative Commons Attribution-NonCommercial 3.0 Unported Licence.

materials. The research aims to explore new insights and indicators through stereological analysis of EBSD data and investigate the interface structure–property relationship of Nd–Fe–B materials from an interfacial perspective.

2. Experimental

This study utilized commercial melt-spun ribbon $Nd_2Fe_{14}B$ powders with the composition $Nd_{13.6}Fe_{73.6}Co_{6.6}Ga_{0.6}B_{5.6}$ (at%) [MQU-F, Magnequench Co.]. The magnetic powders were processed into hot-pressed (HP) magnets using spark plasma sintering (VHPsp-10/25-2500) equipment at 650 °C and 200 MPa. The HP magnet was then deformed at 750 °C in a graphite mold, resulting in a 60% reduction in height. X-ray diffraction (Smartlab SE) was employed to determine the crystal structure, and magnetic properties were measured using a vibrating sample magnetometer with a maximum magnetic field of 3 T (Quantum Design PPMS). EBSD characterization was performed using a scanning electron microscope (Thermo Scientific Apreo 2C), equipped with an EDAX Hikari high-speed detector. To ensure measurement accuracy, a step size of 60 nm was used, and the total area of the observation region was 900 square micrometers (Fig. 1).

The original EBSD data were analyzed using TSL OIM Analysis 7.3 software. Pole figures (PF), inverse pole figures (IPF), and orientation distribution functions (ODF) were used to quantify the texture intensity of $Nd_2Fe_{14}B$ grains. Since Nd-rich compounds exhibit complex compositions, including symmetries such as fcc, dhcp, and even potential amorphous structures under certain conditions, this study simplified them to a hypothetical phase with the same tetragonal symmetry as the main $Nd_2Fe_{14}B$ phase. Although this assumption is not entirely appropriate and may lead to errors, it provides an intuitive method for studying the characteristics of Nd/Nr phase boundaries at the current stage. If both phases on either side of the grain boundary were $Nd_2Fe_{14}B$, the boundary was classified as an Nd/Nd boundary. If the phases on both sides of the grain boundary were $Nd_2Fe_{14}B$ and Nd-rich, the boundary was classified as an Nd/Nr boundary. The study employed the five parameter analysis (FPA) method for grain boundary plane distribution analysis,[18] and the FPA code is developed by Carnegie Mellon University.[19] The FPA method had two calculation modes: $\lambda(n)$, which represents the texture of the habit plane assuming no misorientation, and $\lambda(\Delta g, n)$, which represents the texture of the grain boundary plane with a specific misorientation. For tetragonal symmetry, $45*10^4$ traces were required for the $\lambda(\Delta g, n)$ mode, and $1*10^4$ traces for the $\lambda(n)$ mode. Each analysis of $\lambda(\Delta g, n)$ and $\lambda(n)$ in this study contained sufficient data, ensuring the reliability of the results. Finally, the theoretical geometric positions of the preferred misorientation angles were calculated using the GB Toolbox crystallography program.[20]

3. Results

3.1 Magnetic properties and XRD analysis

Fig. 2a shows the hysteresis loops of the $Nd_2Fe_{14}B$ permanent magnets. For the HP $Nd_2Fe_{14}B$ permanent magnet, the remanence (M_r) was 8.1 kG, the coercive (H_{cj}) was 21.1 kOe, and the maximum energy product [$(BH)_{max}$] was 14.0 MGOe. For the HD $Nd_2Fe_{14}B$ permanent magnet, M_r was 12.2 kG, H_{cj} was 16.4 kOe, and $(BH)_{max}$ was 34.9 MGOe. After deformation, M_r increased by 50.6%, and $(BH)_{max}$ increased by 149.3%. The significant differences in the hysteresis loops indicate that the hot-deformed magnet developed anisotropy. Fig. 2b shows the XRD pattern of the HD $Nd_2Fe_{14}B$ permanent magnet. For comparison, the XRD pattern of the HP permanent magnet is also shown. The intensity ratio of the $I_{(006)}$ to $I_{(105)}$ peaks was used to measure the texture intensity.[21] The $I_{(006)}/I_{(105)}$ ratio was 1.1, further confirming that the HD $Nd_2Fe_{14}B$ permanent magnet forms a strong texture.

3.2 EBSD analysis

To analyze the orientation of the $Nd_2Fe_{14}B$ grains, Fig. 3a shows an Inverse pole figure quick map of the microstructure in the measured region of the HD $Nd_2Fe_{14}B$ permanent magnet. The orientation of each $Nd_2Fe_{14}B$ grain can be determined using the tetragonal crystallographic orientation legend. As shown in the

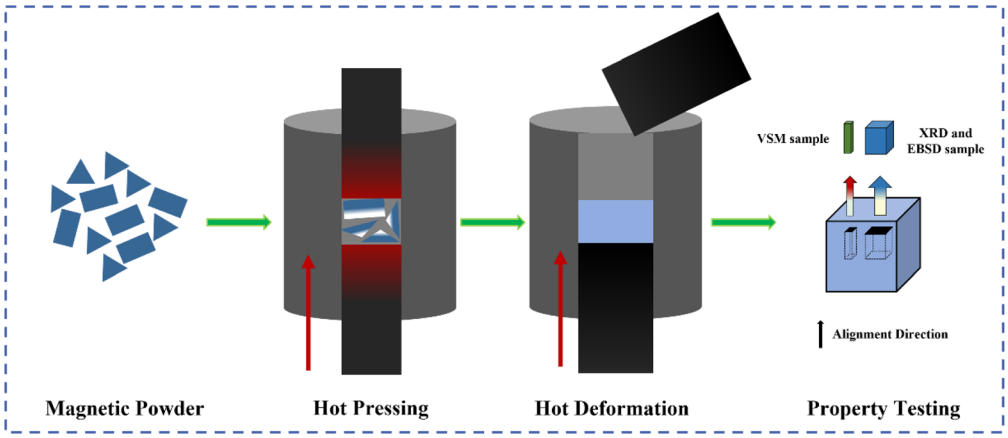

Fig. 1 Preparation process diagram of hot-deformed magnet.

 © 2025 The Author(s). Published by the Royal Society of Chemistry

Open Access Article. Published on 12 May 2025. Downloaded on 10/31/2025 12:40:26 PM.
This article is licensed under a Creative Commons Attribution-NonCommercial 3.0 Unported Licence.

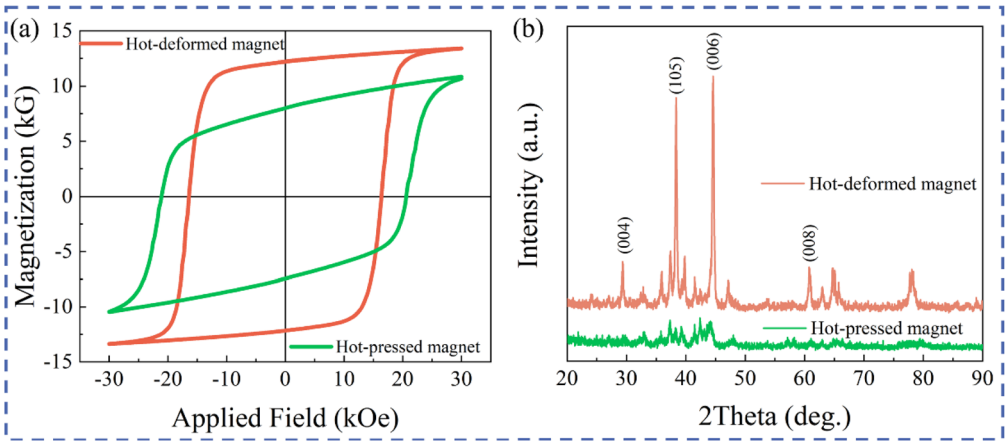

Fig. 2 Hysteresis loops (a) and XRD patterns (b) of $Nd_2Fe_{14}B$ permanent magnet, perpendicular magnet surfaces were obtained.

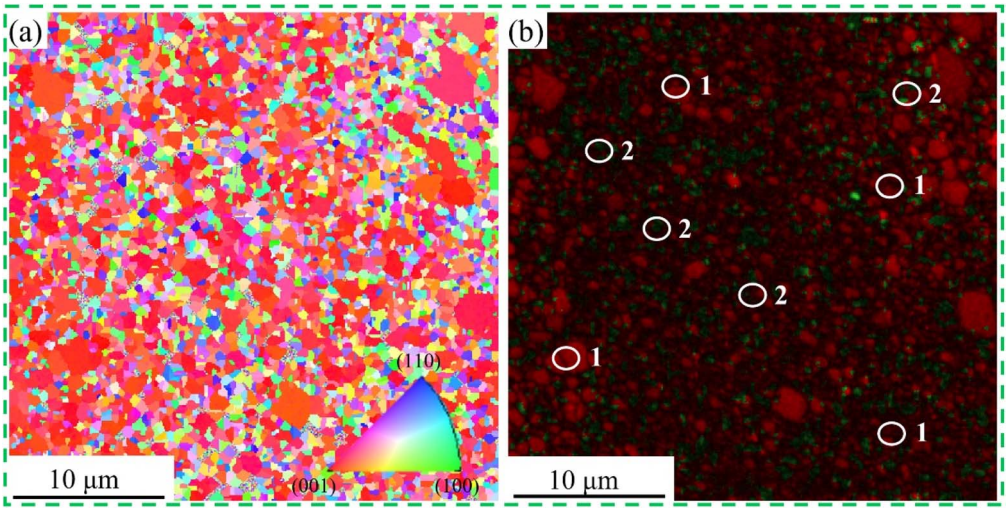

Fig. 3 Inverse pole figure quick map of microstructure in the measurement region of hot-deformed $Nd_2Fe_{14}B$ permanent magnet (a), the phase map of the $Nd_2Fe_{14}B$ permanent magnet imposed on the image quality map, with red color represent the main phase $Nd_2Fe_{14}B$ and green color represent Nd-rich (b).

figure, the $Nd_2Fe_{14}B$ grains exhibit a distinct (001) orientation, consistent with the XRD results (Fig. 2b). Fig. 3b shows the phase map of the $Nd_2Fe_{14}B$ permanent magnet, superimposed on the image quality map. In this representation, the red corresponds to the main $Nd_2Fe_{14}B$ phase, while the green indicates the Nd-rich phase. The boundaries can be classified into $Nd_2Fe_{14}B/Nd_2Fe_{14}B$ boundaries (Nd/Nd boundaries; see white circle (1) and $Nd_2Fe_{14}B$/Nd-rich phase boundaries (Nd/Nr boundaries; see white circle (2), based on the phase distribution map. The distribution characteristics were further analyzed based on the classification of these grain boundaries.

To further analyze the orientation distribution of the $Nd_2Fe_{14}B$ grains, Fig. 4 shows the PF, IPF, and ODF of the HD $Nd_2Fe_{14}B$ permanent magnet. Both the PF and IPF of $Nd_2Fe_{14}B$ grains exhibit a strong {001} orientation texture. The {001} orientation in $Nd_2Fe_{14}B$ grains shows a maximum intensity of 17.3 MRD (Multiples of Random Distribution) (Fig. 4a), while the maximum intensity of the normal direction (ND) orientation in the IPF is also 17.3 MRD (Fig. 4b). Further analysis involved the calculation the ODF of $Nd_2Fe_{14}B$ grains, which shows a maximum intensity of 22.8 MRD, predominantly distributed at $\Phi = 0$ (Fig. 4c). These results indicate that the $Nd_2Fe_{14}B$ grains favor the {001} orientation, demonstrating a strong texture formation.

3.3 Misorientation angle analysis

As the grain boundary plane distribution study begins, it is important to clarify the distribution of misorientation angles at the Nd/Nd and Nd/Nr boundaries (Fig. 5a). The experimental distribution significantly deviates from a random distribution. Two preferred misorientation angles of 45° and 56° were observed for the Nd/Nd boundaries, and two preferred misorientation angles of 45° and 62° were observed for the Nd/Nr boundaries. To investigate the distribution of rotation axes for the misorientation angles of $Nd_2Fe_{14}B$ grains, Fig. 5b shows the axis/angle distribution function maps for the preferred

Open Access Article. Published on 12 May 2025. Downloaded on 10/31/2025 12:40:26 PM.
This article is licensed under a Creative Commons Attribution-NonCommercial 3.0 Unported Licence.

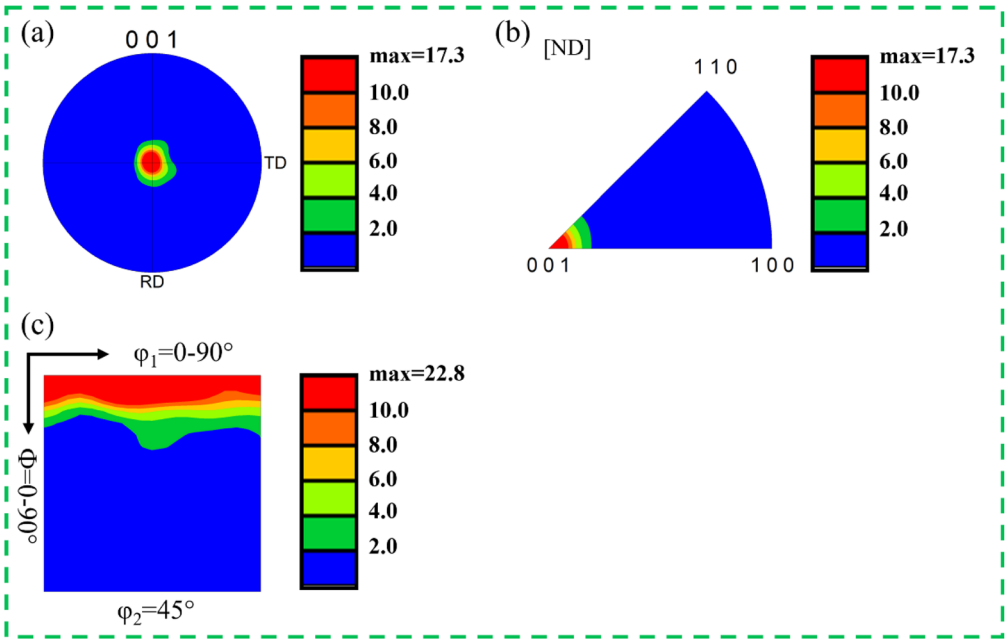

Fig. 4 Pole figure (a), inverse pole figure (b) and orientation distribution function (c) of the hot-deformed $Nd_2Fe_{14}B$ permanent magnet. Orientation texture intensity is given in MRD.

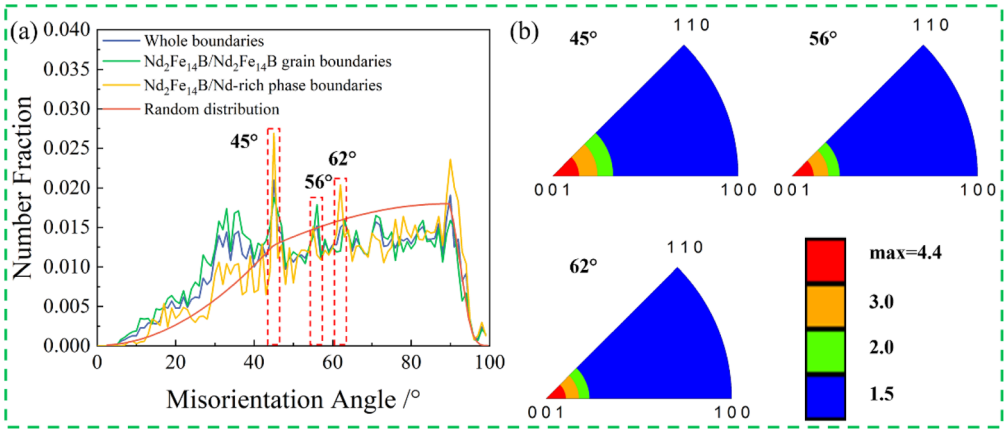

Fig. 5 Misorientation angle distribution of hot-deformed $Nd_2Fe_{14}B$ permanent magnet(a) and axis/angle misorientation distribution functions for hot-deformed $Nd_2Fe_{14}B$ magnet(b). Orientation texture intensity is given in MRD.

misorientation angles. The analysis of the misorientation distribution function of $Nd_2Fe_{14}B$ grains revealed that the [001] axis was the preferred rotation axis for all three groups of misorientation angles. Therefore, three preferred misorientation angle relationships—45°/[001], 56°/[001], and 62°/[001]—were identified. The {001} orientation shows a maximum intensity of 4.4 MRD. It is worth noting that the orientation texture of the $Nd_2Fe_{14}B$ crystals, regardless of specific orientation, is represented by Fig. 5.

Table 1 presents the stereological results for the Nd/Nd and Nd/Nr boundaries. It is significant in that it quantifies the composition and distribution characteristics of these boundaries. Additionally, the wetting process of the Nd-rich phase on the $Nd_2Fe_{14}B$ phase is described. The number fraction, number density, length fraction, and length density at the Nd/Nd and Nd/Nr boundaries are comparable. At the Nd/Nd boundaries, a larger average length indicates closer contact between the $Nd_2Fe_{14}B$ grains, which weakens the exchange coupling between the $Nd_2Fe_{14}B$ phase grains, leading to a decrease in coercivity. In contrast, a larger average length at the Nd/Nr boundaries enhances the wetting of the Nd-rich phase on the $Nd_2Fe_{14}B$ grains. This effective wetting optimizes the orientation of $Nd_2Fe_{14}B$ grains and enhances the remanence of the permanent magnet.

3.4 Grain boundary plane distribution analysis

To describe the grain boundary orientation distribution function (GBP-ODF) of $Nd_2Fe_{14}B$ grains, Fig. 6 shows a map of the

 © 2025 The Author(s). Published by the Royal Society of Chemistry

Open Access Article. Published on 12 May 2025. Downloaded on 10/31/2025 12:40:26 PM.
This article is licensed under a Creative Commons Attribution-NonCommercial 3.0 Unported Licence.

Table 1 Stereological statistics of $Nd_2Fe_{14}B/Nd_2Fe_{14}B$ and $Nd_2Fe_{14}B$/Nd-rich[22]

Name	$Nd_2Fe_{14}B/Nd_2Fe_{14}B$	$Nd_2Fe_{14}B$/Nd-rich
Number fraction (%)	56.26	43.74
Number density (μm^2)	13.98	10.65
Length fraction (%)	56.40	43.60
Length density (μm^2)	1.66	1.26
Average length (μm)	0.12	0.12

GBP-ODF for the three groups of preferred misorientation angles. For the 45°/[001] misorientation angle, the maximum intensity is 4.5, as shown by the MRD values in Fig. 6a. A comparison of the grain boundary plane orientation distribution map (Fig. 6a1) with the geometric feature positions (Fig. 6a2) reveals a significant tilt structure, interspersed with a weak 180°-twist structure. For the 56°/[001] misorientation angle, the maximum intensity is 4.4, as shown by the MRD values in Fig. 6b. A comparison of the grain boundary plane orientation distribution map (Fig. 6b1) with the geometric feature positions (Fig. 6b2) reveals a significant twist structure, interspersed with a weak 180°-tilt structure. For the 62°/[001] misorientation angle, the maximum intensity is 4.9, as shown by the MRD values in Fig. 6c. A comparison of the grain boundary plane orientation distribution map (Fig. 6c1) with the geometric feature positions (Fig. 6c2) reveals a significant 180°-tilt structure for the 62°/[001] misorientation angle. The limitations of the EBSD analysis software made it challenging to identify different types of grain boundary plane orientation distributions.

To describe the distribution characteristics of the grain boundary plane for different types, $\lambda(n)$ analysis was performed on the whole boundaries, Nd/Nd boundaries, and Nd/Nr boundaries along the [001] direction (Fig. 7). The habit plane favored the (011) orientation across whole boundaries, with the maximum value being 3% higher than of random boundaries (Fig. 7a). For Nd/Nd boundaries (Fig. 7b), the habit plane favored the (122) orientation, with the maximum value 5% higher than of random boundaries. For Nd/Nr boundaries (Fig. 7c), the habit plane favored the (012) orientation, with the maximum value 3% higher than of random boundaries. The $\lambda(n)$ value, a key parameter, is typically used to describe the characteristics of a material's properties and behavior, both

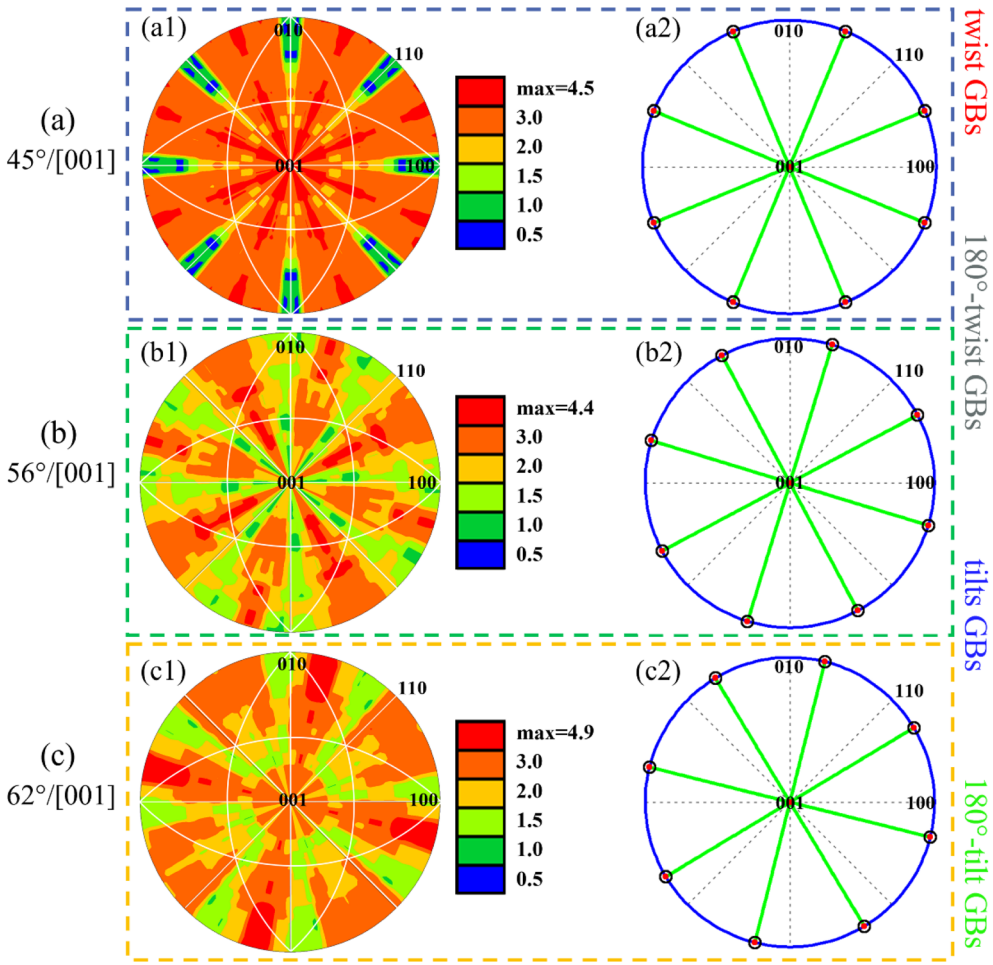

Fig. 6 Grain boundary plane orientation distribution function (GBP-ODF) maps of hot-deformed $Nd_2Fe_{14}B$ permanent magnets and theoretical geometrical feature positions, (a) 45°, (b) 56° and (c) 62°. Orientation texture intensity is given in MRD.

Open Access Article. Published on 12 May 2025. Downloaded on 10/31/2025 12:40:26 PM.
This article is licensed under a Creative Commons Attribution-NonCommercial 3.0 Unported Licence.

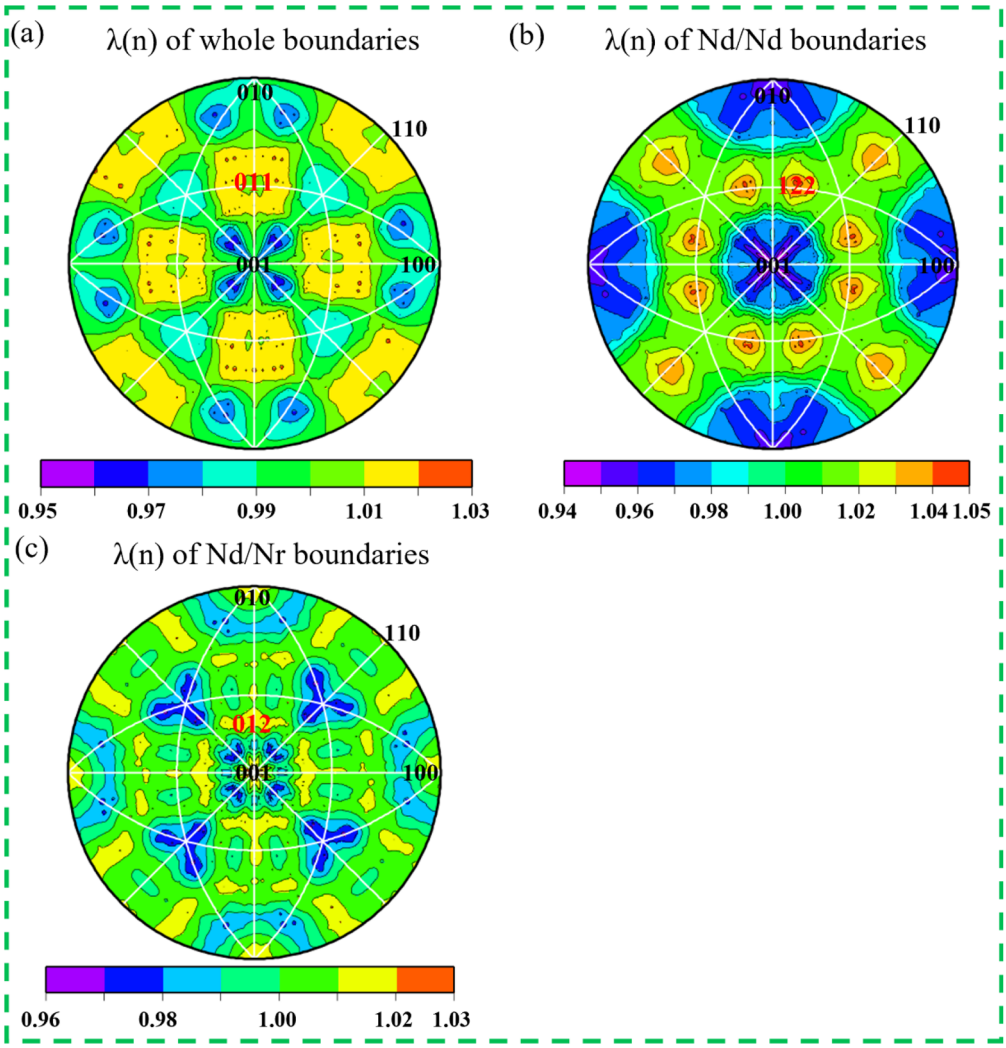

Fig. 7 Orientation distribution of $\lambda(n)$ on the habit plane of hot-deformed $Nd_2Fe_{14}B$ permanent magnets, (a) whole boundaries; (b) Nd/Nd grain boundaries; (c) Nd/Nr phase boundaries. Orientation texture intensity is given in MRD.

within the material and at its boundaries. By comparing the $\lambda(n)$ values of different boundaries, significant differences can be observed. For example, the $\lambda(n)$ value of Nd/Nd boundaries is generally higher than that of the whole boundary, while the $\lambda(n)$ value of Nd/Nr boundaries represents an intermediate state. This difference may arise from variations in atomic arrangement, chemical composition, or crystal structure at different boundaries. Understanding the distribution of various grain boundaries is crucial for elucidating the relationship between a material's internal microstructure and its properties, providing valuable insights for further research.

The $\lambda(\Delta g, n)$ analysis of the preferred misorientation angles at the whole boundaries, Nd/Nd boundaries, and Nd/Nr boundaries is presented in Fig. 8. The $\lambda(\Delta g,n)$ value reflects the physical properties of the Nd–Fe–B material along the [001] direction. Specifically, the $\lambda(\Delta g, n)$ values for the 45°/[001], 56°/[001], and 62°/[001] misorientation angles are compared across the whole boundaries, Nd/Nd boundaries, and Nd/Nr boundaries. For the 45°/[001] misorientation angle at the whole boundaries, the maximum intensity is 1.70 MRD. For the 56°/[001] misorientation angle, the maximum intensity is 1.70 MRD at the {122} position. For the 45°/[001] misorientation angle at the Nd/Nd boundaries, the maximum intensity remains 1.70 MRD. For the 56°/[001] misorientation angle at the Nd/Nd boundaries, the maximum intensity is 1.68 MRD at both the (122) and (100) positions. For the 45°/[001] misorientation angle at the Nd/Nr boundaries, the maximum intensity is 2.20 MRD at the (001) position. Finally, for the 62°/[001] misorientation angle, the maximum intensity is 1.60 MRD at both the (011) and (100) positions.

4. Discussion

This study investigates nanocrystalline Nd–Fe–B magnets, focusing on the key parameter of misorientation angle. Using the FPA method, the orientation distribution characteristics of different boundary types and their correlation with the preferred misorientation angles are systematically explored.

 © 2025 The Author(s). Published by the Royal Society of Chemistry

Open Access Article. Published on 12 May 2025. Downloaded on 10/31/2025 12:40:26 PM.
This article is licensed under a Creative Commons Attribution-NonCommercial 3.0 Unported Licence.

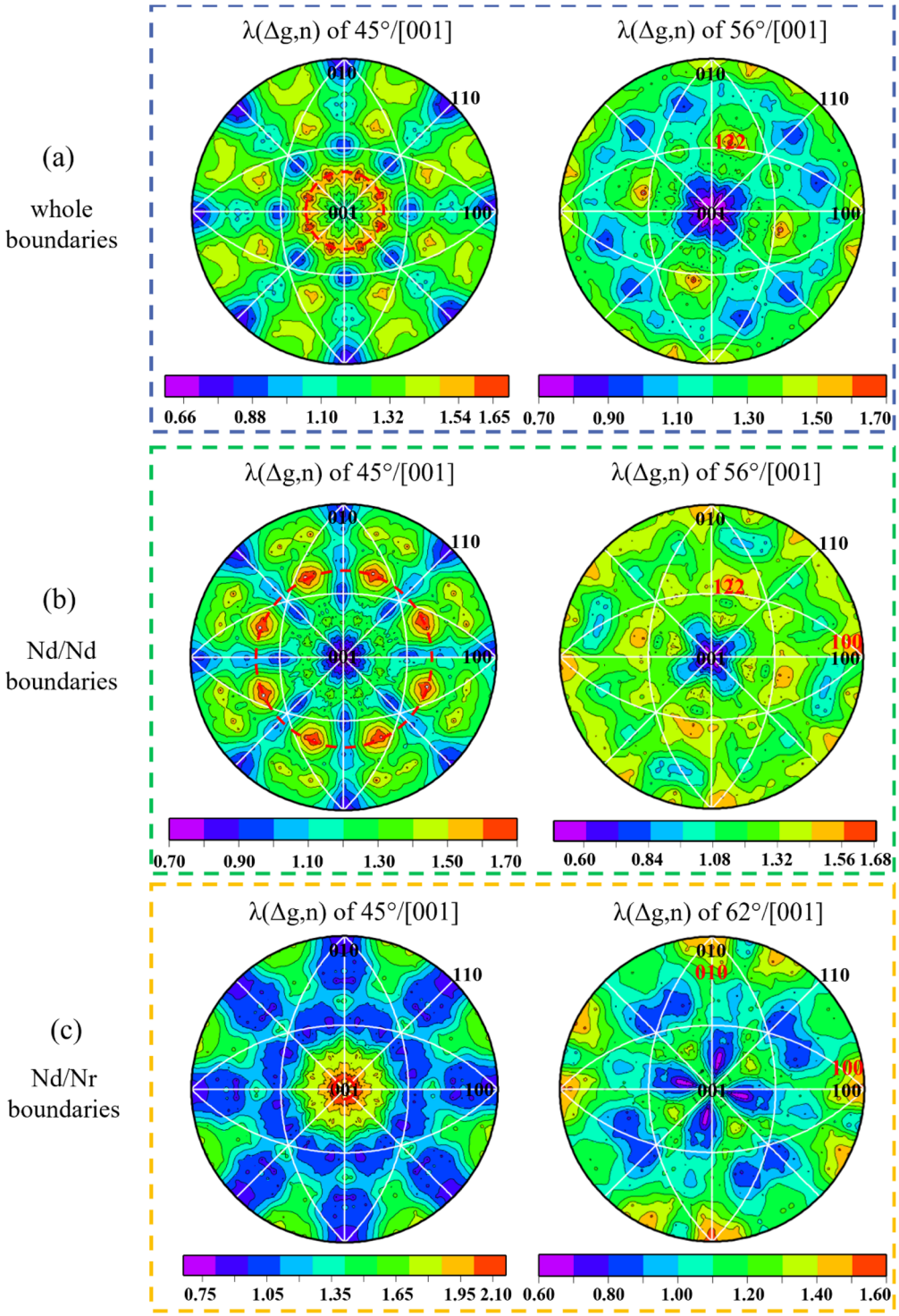

Fig. 8 Orientation distribution of $\lambda(\Delta g, n)$ for hot-deformed $Nd_2Fe_{14}B$ permanent magnets, (a) whole boundaries; (b) Nd/Nd grain boundaries; (c) Nd/Nr phase boundaries. Orientation texture intensity is given in MRD.

The following sections provide an in-depth analysis of two core issues.

Firstly, regarding the influence of the $\lambda(n)$ distribution on magnetic properties, Fig. 7 clearly demonstrates that the three groups of boundary orientation distributions do not significantly favor the (001) orientation, as their maximum intensity values remain relatively low (only 1.05). Notably, in the core region of the boundary orientation distribution, the (001) orientation exhibits a low-intensity characteristic, with a maximum intensity of approximately 0.95—lower than the theoretical value for a random distribution (1.0). These low-intensity distribution values are consistent with the measured

Open Access Article. Published on 12 May 2025. Downloaded on 10/31/2025 12:40:26 PM.
This article is licensed under a Creative Commons Attribution-NonCommercial 3.0 Unported Licence.

results for remanence (12.2 kG), the $I_{(006)}/I_{(105)}$ peak intensity ratio (1.1), and pole figure intensity (17.3 MRD). Therefore, to optimize magnetic properties—particularly to enhance remanence and the maximum energy product—it is crucial to promote the formation of a more concentrated distribution of the (001) orientation and achieve higher intensity values.

Secondly, regarding the regulatory effect of the $\lambda(\Delta g, n)$ distribution on magnetic properties, this study uses the preferred misorientation angles (45°, 56°, and 62°) as representative cases and thoroughly analyzes the ODF of the corresponding boundaries. Specifically, for the 45° misorientation angle at the whole boundaries, the maximum intensity is concentrated in a circular (001) orientation. However, the circular distribution of the maximum intensity at the 45° Nd/Nd grain boundaries deviates from the (001) orientation, while the circular distribution of the maximum intensity at the 45° Nd/Nr phase boundaries tends toward the (001) orientation. This observation suggests that Nd/Nd grain boundaries, which deviate from the (001) orientation, may hinder the achievement of high remanence, indicating that the *c*-axis orientation of Nd–Fe–B grains has not yet reached the ideal arrangement. Since Nd-rich phase boundaries are treated in this study as a phase with a similar structure to the Nd–Fe–B phase, the concentrated distribution of Nd/Nr phase boundaries partially reflects a good coupling effect between the Nd–Fe–B phase and the Nd-rich phase, which helps to maintain high coercivity. It is noteworthy that the Nd/Nr phase boundaries contain low refractive index crystal planes, such as (001) and (010), which contribute to enhanced coercivity due to their strong surface energy anisotropy.[23–25] Further analysis of the distribution characteristics of the 56° misorientation angle reveals that the orientation distributions of the whole boundaries and the Nd/Nd grain boundaries are similar. This supports the conclusion that the Nd/Nd grain boundaries inherit the distribution characteristics of the whole boundaries, with similar maximum intensity values further confirming this. Therefore, based on the $\lambda(\Delta g, n)$ distribution characteristics, to improve remanence, it is crucial to promote a preference for the (001) orientation at the Nd/Nd grain boundaries to enhance the ordered arrangement of Nd–Fe–B grains. To optimize coercivity, the Nd/Nr phase boundaries should also be concentrated around the (001) orientation to maintain a strong coupling effect.

Based on the above analyses, the distribution of grain boundary has a significant effect on the magnetic properties, especially the distribution of (001) orientation. Promoting a centralized distribution of (001) orientation is essential to increase the remanence and maximum energy product. The distribution characteristics of Nd/Nd grain boundaries and Nd/Nr phase boundaries have an important influence on the coercivity, and good coupling effects help to maintain high coercivity. In the future, continued attention should be paid to the interactions between the (001) orientation and various types of boundaries. In addition, significant differences in the values of $\lambda(n)$ and $\lambda(\Delta g, n)$ across different boundaries further emphasize the complexity of the relationship between the internal microstructure and the material properties. These varying patterns not only deepen our understanding of the material's physical properties but may also offer new insights and strategies for material design and processing. By employing the FPA method, we analyzed the orientation distribution of each grain boundary in detail and identified potential correlations between the whole boundaries, Nd/Nd grain boundaries, and Nd/Nr phase boundaries. These findings provide valuable guidance for the preparation of high-texture, hot-deformed Nd–Fe–B magnets.

5. Summary

This study comprehensively characterized the grain boundary plane distribution in HD $Nd_2Fe_{14}B$ permanent magnets, exploring the potential relationship between grain boundary planes and material properties from a stereological perspective. The following conclusions can be drawn:

(1) HD $Nd_2Fe_{14}B$ magnets exhibit Nd/Nd boundaries with preferred misorientation angles of 45° and 56°, while Nd/Nr boundaries show preferred misorientation angles of 45° and 62°.

(2) The habit plane for the whole boundaries favors the (011) orientation, for Nd/Nd boundaries it favors the (122) orientation, and for Nd/Nr boundaries it favors the (012) orientation.

(3) The 45° grain boundary plane favors the (001) orientation, the 56° grain boundary plane favors the (122) orientation, and the 62° grain boundary plane favors the (010) orientation.

(4) Optimizing the structural homogeneity of Nd/Nd and Nd/Nr boundaries can enhance the magnetic properties of HD $Nd_2Fe_{14}B$ magnets.

Data availability

Data will be made available on request.

Author contributions

Qian Li: data curation, writing – original draft preparation. Yuan Teng: supervision.

Conflicts of interest

The authors declare that they have no known competing financial interests.

Acknowledgements

We are grateful to Prof. Yue Ming, Prof. Zhang Dongtao for their help in the research of ideas and computational characterization equipment.

References

1 X. C. Kou, E. H. C. P. Sinnecker and R. Grössinger, Determination of the magnetocrystalline anisotropy of R–T compounds with the easy magnetization direction perpendicular to the c-axis, *J. Magn. Magn. Mater.*, 1996, **157–158**, 83–84.

 © 2025 The Author(s). Published by the Royal Society of Chemistry

Open Access Article. Published on 12 May 2025. Downloaded on 10/31/2025 12:40:26 PM.
This article is licensed under a Creative Commons Attribution-NonCommercial 3.0 Unported Licence.

2 V. E. Zhivulin, O. V. Zaitseva, E. A. Trofimov, N. S. Zabeivorota, M. V. Gavrilyak, F. V. Podgornov, D. A. Vinnik, M. A. Almessiere, Y. Slimani, A. Baykal, K. A. Astapovich and A. V. Trukhanov, Anisotropy of the electrical properties of a single crystal of $BaFe_{11.25}Ti_{0.75}O_{19}$ M-type barium hexaferrite, *J. Solid State Chem.*, 2021, **298**, 122104.

3 Q. Zhao, X. X. He, F. J. Morvan, X. F. Zhang, G. P. Zhao, Z. B. Li and Q. Ma, The influence of interface anisotropy on demagnetization progress and magnetic properties in parallelly oriented hard/soft exchange-coupled multilayers, *J. Magn. Magn. Mater.*, 2019, **476**, 40–44.

4 P. Corte-Leon, V. Zhukova, J. M. Blanco, M. Ipatov, S. Taskaev, M. Churyukanova, J. Gonzalez and A. Zhukov, Engineering of magnetic properties and magnetoimpedance effect in Fe-rich microwires by reversible and irreversible stress-annealing anisotropy, *J. Alloy. Compd.*, 2021, **855**, 157460.

5 G. B. Han, R. W. Gao, S. S. Yan, H. Q. Liu, S. Fu, W. C. Feng, W. Li and X. M. Li, Effect of exchange–coupling interaction on the effective anisotropy in nanocrystalline $Nd_2Fe_{14}B$ material, *J. Magn. Magn. Mater.*, 2004, **281**, 6–10.

6 B. Wolf, Ch. Thurn, L. Postulka, S. K. Thallapaka, U. Tutsch, F. Ritter, C. Krellner and M. Lang, Magnetic and magneto-elastic couplings in the low-dimensional Heisenberg quantum magnet $Cs_2CuCl_2Br_2$ with octahedral Cu coordination, *J. Magn. Magn. Mater.*, 2019, **480**, 108–111.

7 Z. X. Wang, K. Pei, J. J. Zhang, R. J. Chen, W. X. Xia, J. Z. Wang, M. Li and A. R. Yan, Correlation between the microstructure and magnetic configuration in coarse-grain inhibited hot-deformed NdFeB magnets, *Acta Mater.*, 2019, **167**, 103–111.

8 X. K. Yuan and J. Zhu, Anisotropic Distribution of Phase Boundaries and its Potential Correlation with Magnetic Properties in a Sintered NdFeB Permanent Magnet, *Phys. Status Solidi B*, 2020, **257**, 1900326.

9 G. Obara, H. Yamamoto, M. Tani and M. Tokita, Magnetic properties of spark plasma sintering magnets using fine powders prepared by mechanical compounding method, *J. Magn. Magn. Mater.*, 2002, **239**, 464–467.

10 M. Omori, Sintering, consolidation, reaction and crystal growth by the spark plasma system (SPS), *Mater Sci Eng A*, 2000, **287**, 183–188.

11 Y. Q. Li, X. C Xu, M. Yue, T. Y. Ma and W. Q. Liu, Correlation between microstructural heterogeneity and energy product in hot deformed Nd–Fe–B magnets, *J. Magn. Magn. Mater.*, 2020, **508**, 166847.

12 W. J. Mo, L. T. Zhang, A. D. Shan, L. J. Cao, J. S. Wu and M. Komuro, Microstructure and magnetic properties of NdFeB magnet prepared by spark plasma sintering, *Intermetallics*, 2007, **15**(11), 1483–1488.

13 M. Leonowicz, D. Derewnicka, M. Wozniak and H. A. Davies, Processing of high performance anisotropic permanent magnets by die-upset forging, *J. Mater. Process. Technol.*, 2004, **153–154**, 860–867.

14 T. G. Woodcock and O. Gutfleisch, Multi-phase EBSD mapping and local texture analysis in NdFeB sintered magnets, *Acta Mater.*, 2011, **59**(3), 1026–1036.

15 S. Sawatzki, T. G. Woodcock, K. Güth, Müller, K. H. Mueller and O. Gutfleisch, Calculation of remanence and degree of texture from EBSD orientation histograms and XRD rocking curves in Nd–Fe–B sintered magnets, *J. Magn. Magn. Mater.*, 2015, **382**, 219–224.

16 X. C. Xu, Y. Q. Li, Y. Teng, T. Wang, H. G. Zhang, D. T. Zhang and M. Yue, Bulk anisotropic nanocrystalline $Sm_{0.6}Pr_{0.4}Co_5$ magnets with excellent energy density, *Mater. Charact.*, 2021, **173**, 110942.

17 Q. F. Huang, Q. Z. Jiang, J. F. Hu, S. U. Rehman, G. Fu, Q. C. Quan, J. X. Huang, D. Q. Xu, D. K. Chen and Z. C. Zhong, Extraordinary simultaneous enhancement of the coercivity and remanence of dual alloy HRE-free Nd–Fe–B sintered magnets by post-sinter annealing, *J. Mater. Sci. Technol.*, 2022, **106**, 236–242.

18 D. M. Saylor, B. S. El-Dasher, B. L. Adams and G. S. Rohrer, Measuring the five-parameter grain-boundary distribution from observations of planar sections, *Metall. Mater. Trans. A*, 2004, **35**, 1981–1989.

19 **http://imim.p/personal/adam.morawiec**.

20 K. Glowinski and A. Morawiec, Twist, tilt, and symmetric grain boundaries in hexagonal materials, *J. Mater. Sci.*, 2014, **49**, 3936–3942.

21 X. C. Xu, H. G. Zhang, T. Wang, Y. Q. Li, D. T. Zhang and M. Yue, Local orientation texture analysis in nanocrystalline $Sm_{0.6}Pr_{0.4}Co_5$ magnet and $(SmCo_5)_{0.6}(PrCo_5)_{0.4}$ composite magnet with strong magnetic anisotropy, *J. Alloy. Compd.*, 2017, **699**, 262–267.

22 X. K. Yuan, S. X. Zhao, C. B. Wei and X. W. Liu, Misorientations across interfaces in spark plasma–sintered WC–Co cemented carbides, *J. Am. Chem. Soc.*, 2025, **108**(2), e20218.

23 E. R. Leite, T. R. Giraldi, F. M. Pontes, E. Longo, A. Beltrán and J. Andrés, Crystal growth in colloidal tin oxide nanocrystals induced by coalescence at room temperature, *Appl. Phys. Lett.*, 2003, **83**(8), 1566–1568.

24 Y. B. Wang, B. Q. Li, M. L. Sui and S. X. Mao, Deformation-induced grain rotation and growth in nanocrystalline Ni, *Appl. Phys. Lett.*, 2008, **92**(1), 011903.

25 R. Theissmann, M. Fendrich, R. Zinetullin, G. Guenther, G. Schierning and D. E. Wolf, Crystallographic reorientation and nanoparticle coalescence, *Phys. Rev. B: Condens. Matter Mater. Phys.*, 2008, **78**(20), 205413.